Atmos. Chem. Phys., 14, 4515–4530, 2014
www.atmos-chem-phys.net/14/4515/2014/
doi:10.5194/acp-14-4515-2014

Atmospheric Chemistry and Physics Open Access

Role of the residual layer and large-scale subsidence on the development and evolution of the convective boundary layer

E. Blay-Carreras[1], D. Pino[1,2], J. Vilà-Guerau de Arellano[3], A. van de Boer[3], O. De Coster[3], C. Darbieu[4], O. Hartogensis[3], F. Lohou[4], M. Lothon[4], and H. Pietersen[3]

[1]Department of Applied Physics, Universitat Politècnica de Catalunya·BarcelonaTech, Barcelona, Spain
[2]Institute of Space Studies of Catalonia (IEEC-UPC), Barcelona, Spain
[3]Meteorology and Air Quality Group, Wageningen University, Wageningen, the Netherlands
[4]Laboratoire d'Aérologie, Université de Toulouse and CNRS, Toulouse, France

Correspondence to: E. Blay-Carreras (estel.blay@upc.edu)

Abstract. Observations, mixed-layer theory and the Dutch Large-Eddy Simulation model (DALES) are used to analyze the dynamics of the boundary layer during an intensive operational period (1 July 2011) of the Boundary Layer Late Afternoon and Sunset Turbulence campaign. Continuous measurements made by remote sensing and in situ instruments in combination with radio soundings, and measurements done by remotely piloted aircraft systems and two manned aircrafts probed the vertical structure and the temporal evolution of the boundary layer during the campaign. The initial vertical profiles of potential temperature, specific humidity and wind, and the temporal evolution of the surface heat and moisture fluxes prescribed in the models runs are inspired by some of these observations.

The research focuses on the role played by the residual layer during the morning transition and by the large-scale subsidence on the evolution of the boundary layer. By using DALES, we show the importance of the dynamics of the boundary layer during the previous night in the development of the boundary layer at the morning. DALES numerical experiments including the residual layer are capable of modeling the observed sudden increase of the boundary-layer depth during the morning transition and the subsequent evolution of the boundary layer. These simulations show a large increase of the entrainment buoyancy flux when the residual layer is incorporated into the mixed layer. We also examine how the inclusion of the residual layer above a shallow convective boundary layer modifies the turbulent kinetic energy budget.

Large-scale subsidence mainly acts when the boundary layer is fully developed, and, for the studied day, it is necessary to be considered to reproduce the afternoon observations.

Finally, we also investigate how carbon dioxide (CO_2) mixing ratio stored the previous night in the residual layer plays a fundamental role in the evolution of the CO_2 mixing ratio during the following day.

1 Introduction

The atmospheric boundary layer, characterized by a clear diurnal cycle, has been intensively studied since the 1970s. During the day with fair weather conditions, a convective boundary layer (CBL) exists. The physical processes associated to the CBL development have been extensively studied. Sorbjan (1996), Sullivan et al. (1998) and Conzemius and Fedorovich (2006) studied the role of the entrainment processes; Moeng and Sullivan (1994), Fedorovich et al. (2001), Fedorovich et al. (2001), Pino et al. (2003), Pino et al. (2006a) and Pino and Vilà-Guerau de Arellano (2008) the contribution of shear in the generation and maintenance of CBL. Moreover, Yi et al. (2001), de Arellano et al. (2004), Casso-Torralba et al. (2008) and Vilà-Guerau de Arellano et al. (2009) studied the influence of CBL evolution on the carbon dioxide (CO_2) or isoprene budget.

Several methodologies have been used to study the CBL: large eddy simulation (LES) numerical experiments (Moeng, 1984; Nieuwstadt and Brost, 1986; Cuijpers and Duynkerke, 1993; Sorbjan, 2007), mixed-layer model (MLM) (Tennekes, 1973; Tennekes and Driedonks, 1981; Fedorovich, 1995; Pino et al., 2006a), observations (Kaimal et al., 1976; Angevine et al., 1994; Cohn and Angevine, 2000) and

laboratory experiments (Deardorff et al., 1980; Fedorovich et al., 1996).

During the night, a shallower stable boundary layer (SBL) with less turbulence intensity exists near the surface (Nieuwstadt, 1984; Carlson and Stull, 1986; Mahrt, 1998; Beare et al., 2006). Between this layer and the free atmosphere (FA), there may exist a neutrally stratified layer resulting from the decay of turbulence of the previous day CBL. This layer, called the residual layer (RL), appears before sunset, when eddies have less energy due to the reduction of surface fluxes. The RL has the same characteristics in the state variables as the original CBL (Stull, 1988). The importance and the role of the RL was studied by some authors (Balsley et al., 2007; Wehner et al., 2010) who examined turbulence in the RL by analyzing the Richardson number gradient or to explain aerosol formation. Emeis and Schäfer (2006) by using different instruments (e.g., sodar and ceilometer) measured and studied the heights of RL, CBL and SBL and their influence on urban air quality and pollution.

The evolution from CBL to SBL and vice versa happens through two transitional processes. These two periods are difficult to study due to their rapid variability. The afternoon transition has been studied by using observations and/or numerical simulations (Sorbjan, 1997; Cole and Fernando, 1998; Edwards et al., 2006; Pino et al., 2006a; Angevine, 2007; Nadeau et al., 2011). However, there are still many unknowns during this period: the presence of significant vertical movements in late afternoon, which appear even with very small surface heat flux; the influence of boundary layer processes in the turbulence decay; and what the processes are that govern the decrease of the boundary-layer depth (Lothon et al., 2014).

Regarding the morning transition, Angevine et al. (2001), Lapworth (2006), Bange et al. (2006) and Angevine (2007) investigated by using observations the timing and importance of entrainment and surface winds in the development of CBL. LeMone et al. (2002) analyzed data recorded during CASES-97 to study the warming and moistening of the atmosphere due to boundary-layer depth, wind direction, and surface heterogeneity during this period. Other authors (Sorbjan, 1996; Beare, 2008) analyzed the morning transition by using numerical models, such as LES, to study the relevance of different temperature lapse rate or the importance of domain sizes and grid length or by using MLM to study the impact of the atmospheric boundary layer dynamics on the atmospheric chemistry (Ouwersloot et al., 2012).

Some aspects about the relevance of the RL during the morning transition have been studied by Fochesatto et al. (2001) and Gibert et al. (2011), who analyzed the dynamical coupling between the CBL and the RL by using lidar measurements. They observed the generation of internal gravity waves when there was a stable and stratified RL or when there was a thermal forcing. They concluded that horizontal wind shear is not enough to observe internal gravity waves. Other authors (Stensrud, 1993; Balin et al., 2004) focused their research on the elevated RL, which is created when a CBL over an elevated terrain is advected over a lower CBL. Moreover, Han et al. (2011) studied the evolution of the CBL when it is covered by a neutral layer after the morning transition. Finally, Doran et al. (2003) and Morris et al. (2010) examined the vertical mixing of different chemical compounds, such as ozone, nitrogen oxide or carbon monoxide during the morning transition.

Here the role of the RL during the morning transition and the role of subsidence during the whole evolution of the convective boundary layer is studied by using observations, mixed-layer theory (Tennekes and Driedonks, 1981) and the Dutch Large-Eddy Simulation model (DALES, Heus et al. (2010)). In contrast with previous studies, by performing a sensitivity analysis on the residual layer and subsidence characteristics, we analyze the importance of these processes on the diurnal evolution of the convective boundary layer. Specifically, our research objectives can be summarized as follows:

1. To study the variations in the evolution of the boundary-layer depth due to the presence of RL and subsidence,

2. To analyze the relevance of considering the characteristics of the previous night in the potential temperature vertical profile and temporal evolution,

3. To observe the sensitivity of turbulent kinetic energy budget during morning transition and the evolution during the day due to RL,

4. To define the influence of RL on the observed evolution of the CO_2 mixing ratio.

We take profit of the observations taken during an intensive observational campaign of the project Boundary Layer Late Afternoon and Sunset Turbulence (BLLAST; Lothon et al. (2014)). During intensive operational periods (IOPs), more than 30 different instruments provided in situ (nine eddy covariance (EC) stations, towers, balloons, remotely piloted aircraft systems and manned airplanes) and remote sensing (lidar, wind profiler) measurements.

We structure the paper as follows. In Sect. 2, we explain the main characteristics of the field campaign and the instruments selected for this study. Moreover, the numerical setup used in the models is also described in this section. Section 3 shows the results focusing on the evolution of the boundary-layer depth, potential temperature, and turbulent kinetic energy budget to perform the sensitivity analysis. Furthermore, this section analyzes the influence of RL on the observed evolution of the CO_2 mixing ratio. Finally, Sect. 4 summarizes the results.

2 Methodology

2.1 Observations

The observations used here to initialize, drive and qualitatively validate the numerical experiments were recorded during the observational campaign of the BLLAST project (Lothon et al., 2014), from 14 June to 8 July 2011 at Lannemezan (southern France). The main objective of this project is to study the structure and evolution of the boundary layer during the late afternoon transition.

During the whole campaign, ultra-high-frequency (UHF) wind profiler measured vertical velocity with a vertical resolution of 150 m. In a $10 \times 10\,\mathrm{km}^2$ area, EC stations located over different vegetation coverages (short and long grass, wheat and at the edge between long grass and wheat) measured with 10 Hz or 20 Hz frequency acquisition the three wind components, the temperature, the specific humidity and the CO_2 concentration. Particularly, a 60 m tower had EC instruments at 30, 45 and 60 m. Heat, momentum and CO_2 fluxes at surface were estimated at all sites using a uniform processing method (De Coster and Pietersen, 2011).

Among the 19 radiosondes launched between 01:30 UTC and 23:00 UTC on the IOP under study (1 July 2011), we use the ones launched over our area of interest, where the fluxes were measured.

The study is focused on 1 July 2011. This was the second of three consecutive IOPs with increasingly high temperatures. During this IOP, a large high-pressure system was located southwest of the British Islands. The influence of this high-pressure system extends towards the east. This results at the BLLAST site in clear skies, fair weather, and weak wind coming from the north turning to the east during the day at low levels. Higher up in the atmosphere, at 500 hPa, a strong ridge extends over southern Europe causing a predominantly western flow in the region.

2.2 Numerical experiments

Two numerical models of different complexity have been used to study the evolution of the convective boundary layer during the selected day: DALES (Heus et al., 2010) and a MLM (Tennekes and Driedonks, 1981). Both models were initialized and driven by observations.

The domain chosen for the DALES numerical experiments has $12.8 \times 12.8 \times 3.056\,\mathrm{km}^3$, and we define 256 points in each direction (50 and 12 m resolution in the horizontal and vertical directions, respectively). This setup has a similar horizontal domain to the campaign site, having also enough vertical resolution to study entrainment processes (Pino et al., 2003, 2006a). Our DALES numerical experiments run for 12.5 h starting at 07:30 UTC, to include the morning transition in the simulations.

For all the numerical experiments performed with both models, the prescribed surface heat fluxes were based on the observations made by five EC stations over different land uses. A sinusoidal evolution of the surface sensible and latent heat fluxes was prescribed. Figure 1 shows the observed temporal evolution on 1 July 2011 of sensible and latent heat fluxes. Additionally, the prescribed evolution to drive DALES numerical experiments is also shown. MLM is driven by the same evolution of surface heat fluxes but starting at 11:00 UTC, when no RL is observed (see below).

To analyze the role played by the RL in the morning evolution of the convective boundary layer, we consider to initialize DALES with two different vertical profiles of potential temperature (θ) and specific humidity (q). To include the residual layer in DALES (RL numerical experiments), we initialize it by following the observations taken by the radio sounding launched at 07:30 UTC. Figure 2 shows the vertical profile of θ, q, wind speed and direction observed at 01:30 and 07:30 UTC and the prescribed vertical profiles used for initializing DALES RL and no-RL numerical experiments.

Table 1 shows the values of the potential temperature, specific humidity and horizontal wind components that define the initial profiles of the DALES and MLM runs. For the RL numerical experiments, we divide the initial vertical profiles of θ and q in three different layers: CBL from surface to $z_{1,0}$, RL from $z_{1,0}$ to $z_{\mathrm{RL},0}$, and FA above $z_{\mathrm{RL},0}$. The potential

Table 1. Based on the observations taken at the BLLAST campaign on 1 July 2011, initial and prescribed values used for DALES (RL and nRL numerical experiments) and MLM of the boundary-layer depth, mixed-layer and residual layer values of the scalars ($\theta_{1,0}$, $\theta_{\mathrm{RL},0}$ and $q_{1,0}$, $q_{\mathrm{RL},0}$), and their corresponding jump at the inversion ($\Delta\theta_{1,0}$, $\Delta\theta_{\mathrm{RL},0}$, $\Delta q_{1,0}$ and $\Delta q_{\mathrm{RL},0}$). γ_i is the FA lapse rate of each variable i. Initial ($u_{1,0}$, $u_{\mathrm{RL},0}$, $v_{1,0}$, $v_{\mathrm{RL},0}$) and geostrophic ($u_{1,0}$, u_g, v_g) wind components are also indicated. Surface fluxes ($\overline{w'\theta'}|_\mathrm{s}$ and $\overline{w'q'}|_\mathrm{s}$) are prescribed as $0.1668\,\sin(\pi(t-5)/12.5)$ and $0.1032\,\sin(\pi(t-5.5)/13.5)$ respectively. Time t goes from 0 (07:30 UTC) to 45 000 s (20:00 UTC).

	RL	nRL	MLM (11:00 UTC)
$\theta_{1,0}$ (K)	293	293	295.5
$\Delta\theta_{1,0}$ (K)	2	5	8
$z_{1,0}$ (m)	210	210	1300
$\theta_{\mathrm{RL},0}$ (K)	295	–	–
$\Delta\theta_{\mathrm{RL},0}$ (K)	9	–	–
$z_{\mathrm{RL},0}$ (m)	1422	–	–
γ_θ ($\mathrm{K\,m^{-1}}$)	0.005	0.005	0.005
$q_{1,0}$ ($\mathrm{g\,kg^{-1}}$)	7.16	7.16	8
$\Delta q_{1,0}$ ($\mathrm{g\,kg^{-1}}$)	−1.66	−5.66	−5
$q_{\mathrm{RL},0}$ ($\mathrm{g\,kg^{-1}}$)	5.50	–	–
$\Delta q_{\mathrm{RL},0}$ ($\mathrm{g\,kg^{-1}}$)	−4.41	–	–
γ_q ($\mathrm{g\,(kg\,m)^{-1}}$)	−0.00035	−0.00035	−0.00035
$u_{1,0}$ ($\mathrm{m\,s^{-1}}$)	−2.95	−2.95	−2.95
$v_{1,0}$ ($\mathrm{m\,s^{-1}}$)	0.52	0.52	0.52
$u_{\mathrm{RL},0}$ ($\mathrm{m\,s^{-1}}$)	−2.95	–	–
$v_{\mathrm{RL},0}$ ($\mathrm{m\,s^{-1}}$)	0.52	–	–
u_g ($\mathrm{m\,s^{-1}}$)	10	10	10
v_g ($\mathrm{m\,s^{-1}}$)	0	0	0

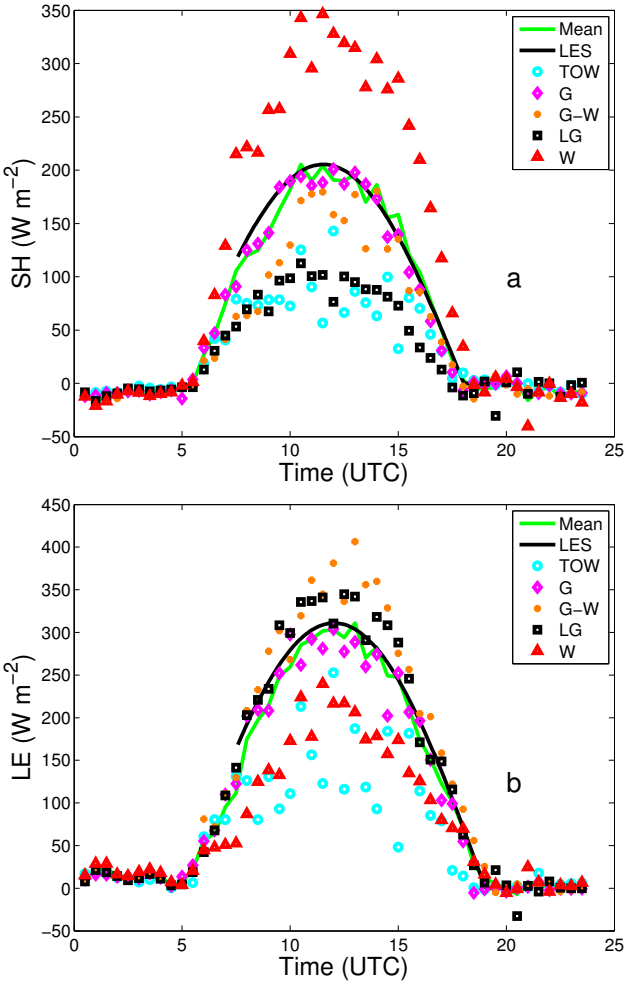

Fig. 1. Temporal evolution of **(a)** sensible and **(b)** latent heat fluxes on 1 July 2011 observed at 2 m (symbols) or 30 m in the tower case and its mean (green line), and prescribed (black line). Observations are from EC instrument at the tower over grass (TOW, cyan circles), over short grass (G, magenta diamonds), over the edge between the long grass and the wheat (G–W, orange dots), over long grass (LG, black squares) and over wheat (W, red triangles).

temperature (specific humidity) in the CBL and in the RL are, respectively, $\theta_{1,0}$ ($q_{1,0}$) and $\theta_{\mathrm{RL},0}$ ($q_{\mathrm{RL},0}$). The inversion jumps at the two boundaries are $\Delta\theta_{1,0}$ ($\Delta q_{1,0}$) and $\Delta\theta_{\mathrm{RL},0}$ ($\Delta q_{\mathrm{RL},0}$). In the FA, the potential temperature (specific humidity) lapse rate is γ_θ (γ_q).

For the numerical experiments without the residual layer (nRL), we divide the initial vertical profiles to run DALES (Fig. 2) in two layers – CBL and FA – and the same notation is used for the CBL values ($\theta_{1,0}$ and $q_{1,0}$) and FA lapse rates (γ_θ and γ_q), being $z_{1,0}$ the initial boundary-layer depth.

LeMone et al. (1999), Pino et al. (2003), and Conzemius and Fedorovich (2006), among others, showed that wind shear at the surface and at the inversion influences the evolution of the CBL. Consequently, we define the initial vertical wind profiles for all the DALES numerical experiments based on the radio sounding observations at 07:30 UTC (see Fig. 2c, d). The initial wind profile is constant with height below the FA, $u_{1,0} = -2.95$, $v_{1,0} = 0.52\,\mathrm{m\,s^{-1}}$, being equal to the geostrophic wind in the FA. Regarding the geostrophic wind, we use the radiosoundings launched during the whole day to prescribe $u_g = 10$, $v_g = 0\,\mathrm{m\,s^{-1}}$, constant with height. The prescribed roughness length, z_0, is 0.1 m and the latitude is $\phi = 43.1°$. Despite the selection of the initial wind profile based on observations, DALES results regarding wind characteristics will not fit the observations (not shown). This is mainly because on 1 July 2011 the dynamics was mainly driven by orography and consequently mountain-valley breezes appeared. DALES numerical experiments do not consider these mesoscale features.

To study the role of subsidence, we perform additional simulations. We obtain the value of subsidence to be included in DALES and MLM numerical experiments, following Yi et al. (2001), by analyzing the observed vertical profile of the potential temperature at 01:30 and 07:30 UTC on 1 July 2011 (see Fig. 2). The depth of the residual layer (z_{RL}) decreases 215 m within 6 hours (01:30–07:30 UTC). This represents an average subsidence velocity of $9.95 \times 10^{-3}\,\mathrm{m\,s^{-1}}$. We include subsidence in two DALES numerical experiments as follows. Subsidence vertical profile increases linearly from 0 at the surface to $9.95 \times 10^{-3}\,\mathrm{m\,s^{-1}}$ at $z_{\mathrm{RL},0}$ in both numerical experiments (RLs and nRLs numerical experiments). In FA, the subsidence is constant and equal to $9.95 \times 10^{-3}\,\mathrm{m\,s^{-1}}$. Despite the fact that subsidence may evolve during the day, we prescribe a constant subsidence profile because the main objective of the paper is not exactly to fit the observations but to analyze the role of RL and subsidence. For this same reason, and taking into account the low winds recorded during the selected IOP, heat, moisture or momentum large-scale advection are not considered.

By combining RL and subsidence, four different DALES numerical experiments were performed: RL with subsidence (RLs), RL without subsidence (RLns), no-RL with subsidence (nRLs) and no-RL without subsidence (nRLns).

MLM is used to create fast and simple characterization of the CBL, and the results can be contrasted with the results of DALES numerical experiments to verify whether simple models can also simulate the evolution of the CBL from midday considering subsidence. The version used here of the MLM does not include the RL in its vertical profile. Consequently, it can only be used for developed convective boundary layers. To initialize MLM, we used the information of the first radio sounding, which shows a completely developed CBL – the one launched at 11:00 UTC. Table 1 shows the values that characterize the MLM initial profile of θ and q. We prescribed in MLM a divergence at $z_{1,0}$, being equal to $7.65 \times 10^{-6}\,\mathrm{s^{-1}}$, obtained by considering the subsidence velocity equal to $9.95 \times 10^{-3}\,\mathrm{m\,s^{-1}}$ and the initial depth of the boundary layer for MLM ($z_{1,0} = 1300$ m).

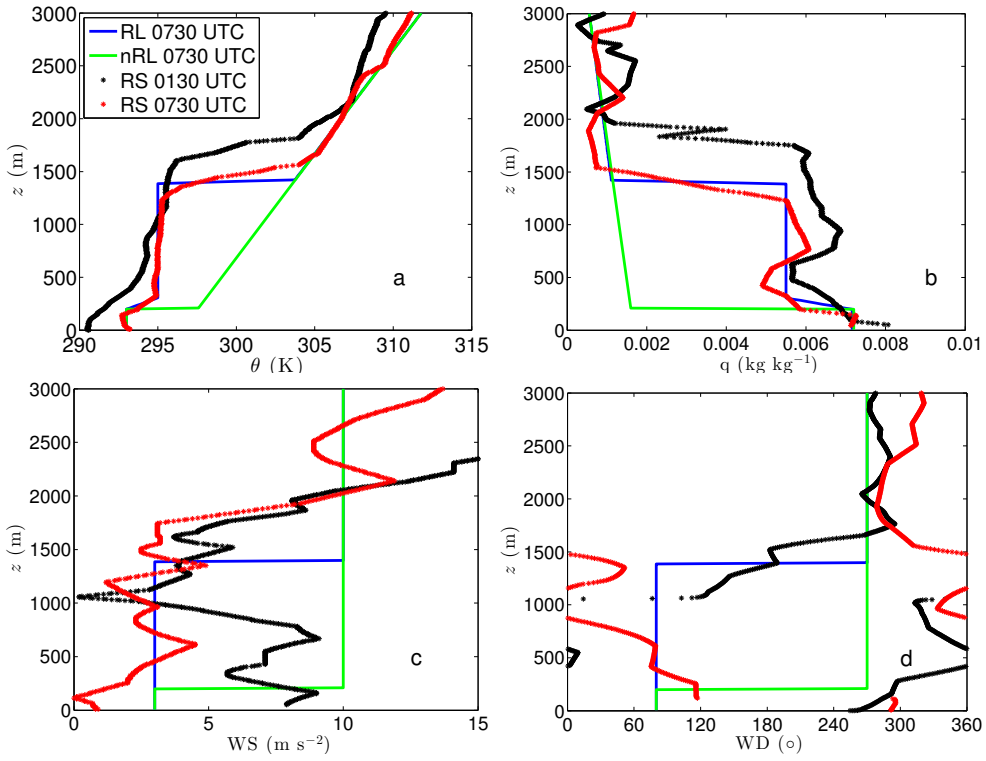

Fig. 2. Vertical profile of **(a)** potential temperature, **(b)** specific humidity, **(c)** wind speed and **(d)** wind direction observed by the radio soundings launched at 01:30 (black dots) and at 07:30 UTC (red dots) on 1 July 2011. Additionally, the vertical profiles based in the observations for initializing the DALES RL numerical experiments (solid blue) and nRL numerical experiments (solid green) are shown. Table 1 shows the values that characterize initial profile of θ, q, u and v.

3 Results

In the next sections, we demonstrate the importance of RL during the morning transition and of subsidence during the afternoon by analyzing the observed and simulated evolution of the boundary-layer depth, potential temperature, turbulent kinetic energy budget and its influence on the evolution of CO_2 mixing ratio.

Mixed-layer theory (Lilly, 1968; Tennekes, 1973; Tennekes and Driedonks, 1981; Carson, 1973) helps us to interpret many of the numerical experiments results. This theory has been proven to correctly describe the evolution of the convective boundary layer (Pino et al., 2003; Conzemius and Fedorovich, 2007). By using mixed-layer theory, if heat advection is considered negligible due to the low winds recorded, the time evolution of the mean potential temperature in the mixed layer ($\overline{\theta}$) in convective conditions is driven by surface and entrainment heat fluxes, and reads

$$\frac{\partial \overline{\theta}}{\partial t} = \frac{\overline{\omega'\theta'}|_s - \overline{\omega'\theta'}|_1}{z_1}, \quad (1)$$

where $\overline{\omega'\theta'}|_s$ and $\overline{\omega'\theta'}|_1$ are the turbulent heat flux at the surface and at z_1 (entrainment heat flux), respectively.

If large-scale subsidence is not considered, zeroth-order mixed-layer theory postulates that entrainment heat flux reads (Lilly, 1968; Tennekes, 1973; Tennekes and Driedonks, 1981; Carson, 1973)

$$\overline{\omega'\theta'}|_1 = -\Delta\theta_1 \frac{\partial z_1}{\partial t}, \quad (2)$$

where $\Delta\theta_1$ is the jump of the potential temperature at the inversion.

3.1 Potential temperature vertical profile

Figure 3 shows the vertical profile of potential temperature observed with the radio soundings, obtained by MLM including subsidence, and obtained by DALES numerical experiments at different hours on 1 July 2011. The figure illustrates the importance of the morning conditions on the evolution of the boundary-layer depth and of the potential temperature during the whole day. At 08:30 UTC (Fig. 3a), when the RL had not yet been incorporated into the boundary layer, mixed-layer potential temperatures in the numerical experiments that consider the RL are 1.7 K lower than nRL numerical experiments, even though the boundary-layer depth is similar, due to the larger potential temperature inversion

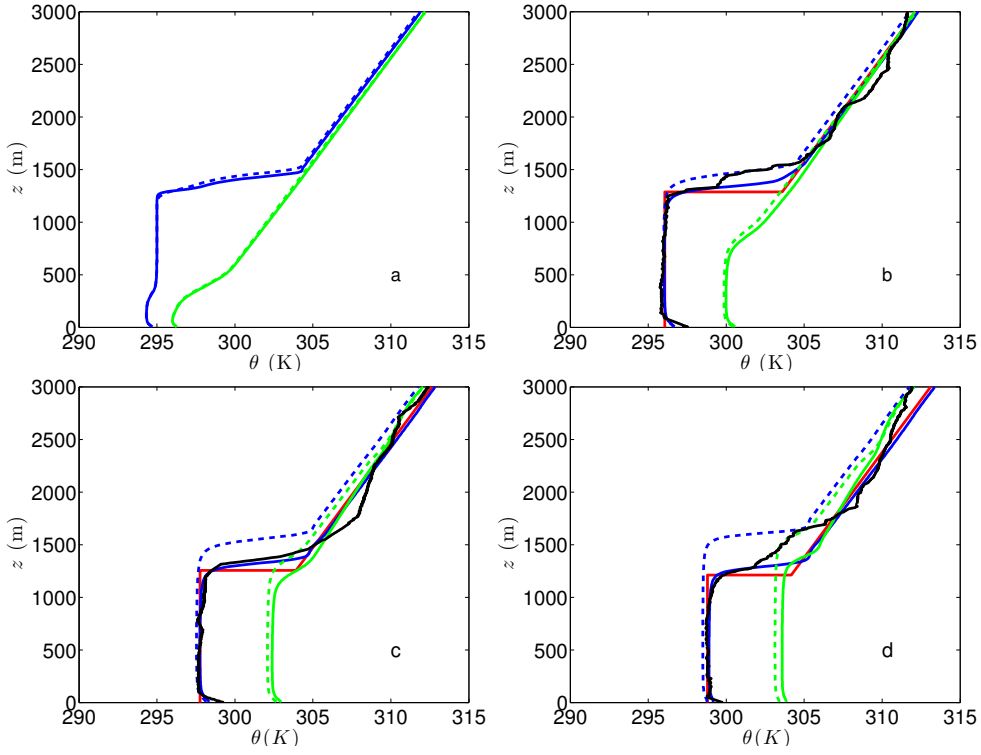

Fig. 3. Vertical profile of the 30-min averaged potential temperature at **(a)** 08:30, **(b)** 11:00, **(c)** 14:00 and **(d)** 17:00 UTC on 1 July 2011 observed by the radio soundings (solid black) and obtained by MLM (solid red) and DALES runs (RLs, solid blue; RLns, dash blue; nRLs, solid green; and nRLns, dash green line).

jump simulated by the nRL numerical experiments, which increases entrainment heat flux (see Eq. 2).

As the day progresses, the difference of mixed-layer θ increases between nRL and RL numerical experiments; RL numerical experiments become approximately 4 K lower than nRL numerical experiments (see Fig. 3b) fitting the observations. As the nRL presents a lower depth of the CBL during a longer period of time, its temperature increases faster reaching higher values during this period. However, after 13:00 UTC when the boundary-layer depth simulated by the nRL numerical experiments reaches around 1300 m, the difference in the mixed-layer potential temperature between RL and nRL numerical experiments is maintained (see Fig. 3c, d) due to the similar values of entrainment heat flux and boundary layer depth simulated for all the numerical experiments. Moreover, the influence of subsidence in the boundary-layer depth and potential temperature is noticeable from midday. RLns and nRLns clearly overestimate the observed boundary-layer depth by several hundred meters, and the potential temperature is 0.5 K colder (see Fig. 3c, d).

3.2 Mixed-layer potential temperature temporal evolution

Figure 4 shows the temporal evolution of potential temperature obtained by the MLM with subsidence and obtained by the four DALES numerical experiments in the middle point between the surface and the height when the heat flux becomes 0 W m^{-2} below z_1. The figure also shows the observed temporal evolution of the 2 m potential temperature over different land uses during 1 July 2011. Notice that measurement height is different to the height where DALES results are considered, what may produce some discrepancies. Differences between potential temperature measurements are below 1 K except for the potential temperature measured over wheat. As it was already pointed out by previous studies (Nadeau et al., 2011, among others), surface heat flux over wheat is larger (Fig. 1a) yielding larger 2 m potential temperature.

If the residual layer is not considered (nRLs and nRLns numerical experiments), the simulated 2 m potential temperature increases rapidly due to the initially prescribed large potential temperature jump, which increases the entrainment heat flux. Moreover, the CBL is shallow during the morning (Fig. 3a, b) enhancing the CBL-heating rate (see Eqs. 1 and 2). Consequently, these DALES runs do not fit the observations.

On the contrary, if the residual layer is included in the initial profile of DALES numerical experiments, the temporal evolution of mixed-layer potential temperature presents two different regimes. For approximately the first 1.5 h of

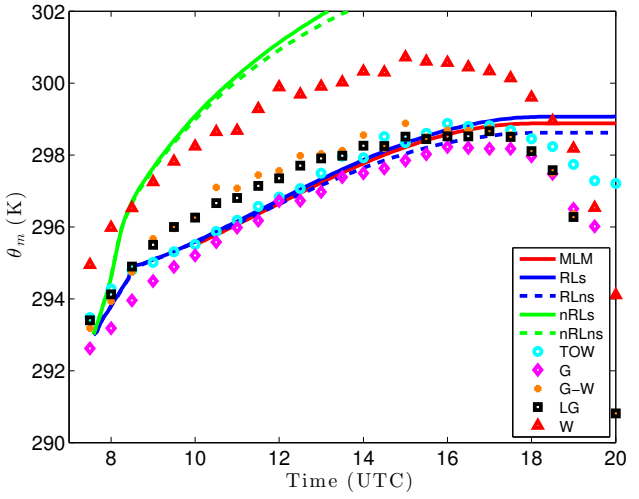

Fig. 4. Temporal evolution of potential temperature on 1 July 2011 observed by different instruments at 2 m (symbols) and obtained (lines) by MLM with subsidence (red) and DALES (RLs, solid blue; RLns, dash blue; nRLs, solid green; and nRLns, dash green). Observations are from EC instrument at the tower over grass (TOW, cyan circles), over short grass (G, magenta diamonds), over the edge between the long grass and the wheat (G–W, orange dots), over long grass (LG, black squares) and over wheat (W, red triangles).

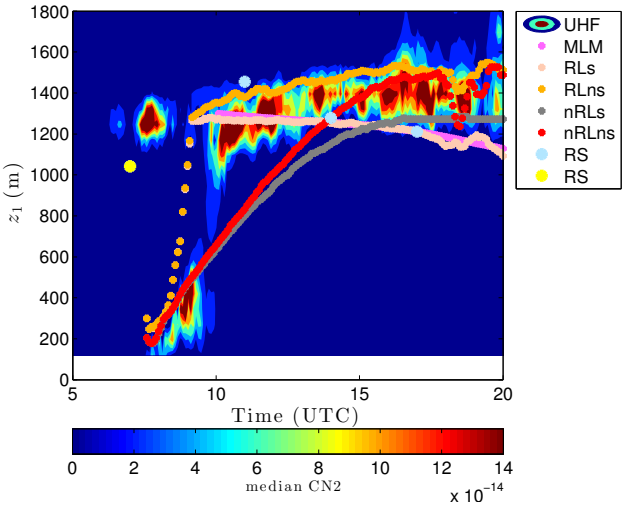

Fig. 5. Temporal evolution during 1 July 2011 of the refractive structure coefficient measured by UHF wind profiler (color contour), and boundary layer depth estimated from radio soundings (light blue dots), and obtained by MLM (magenta line), and DALES runs (RLs, pink; RLns, orange; nRLs, grey; and nRLns, red lines). Yellow dot represents the residual layer depth estimated from a radio sounding.

the simulation, the boundary layer is shallow, but the inversion layer jump is moderate when compared with the nRL numerical experiments. Consequently, entrainment heat flux is smaller and potential temperature increases smoothly, approximately fitting the observations. At 09:00 UTC, when the potential temperature in the mixed layer and in the residual layer are the same, the boundary-layer depth increases approximately to 1300 m. Although the new potential temperature inversion jump is larger, the heating rate is lower compared with the first 1.5 h of simulation due to the large z_1 simulated at this moment, and DALES RL numerical experiments fit better the observations.

Once the mixed layer has incorporated the residual layer, MLM considering subsidence starting at 11:00 UTC simulates correctly the evolution of the potential temperature, being close to the observed values and to the results of DALES runs that take into account the residual layer.

The role played by subsidence in the evolution of the potential temperature can be only appreciated at the end of the afternoon. This is due to several reasons. Taking into account how subsidence is prescribed, its effects are very small if $z_1 < z_{RL,0}$, that is, before 10:00 UTC or 16:00 UTC for RL and nRL numerical experiments, respectively. Moreover, in the afternoon, the surface, and as a consequence the entrainment, heat flux largely reduces, decreasing the boundary layer growth. However, none of the numerical experiments is able to simulate the decrease of potential temperature observed from 17:00 UTC, which maybe is produced by a weak negative heat advection due to the change in wind direction produced by slope flows.

3.3 Boundary-layer depth temporal evolution

Figure 5 shows the time evolution of the refractive structure coefficient (CN2) observed by the UHF wind profiler and the boundary layer depth estimated from the radio soundings launched at 07:30, 11:00, 14:00, 17:00, and 20:00 UTC, and obtained by MLM with subsidence and by DALES numerical experiments (RLs, RL, nRLs and nRL). z_1 for MLM and DALES is defined as the height where the minimum buoyancy flux occurs (Seibert et al., 2000). z_1 obtained from the radio sounding data is defined as the height where the maximum virtual potential temperature gradient occurs. The reliability to obtain the depth of the boundary layer by using isolated radio soundings has been sometimes criticized (e.g., Stull 1988). Nevertheless, radio sounding measurements in this study fit correctly with the UHF measurements, and the small dissimilarities can be attributed to the different procedures used to obtain z_1 (Sullivan et al., 1998).

UHF wind profiler measurements show the existence of a residual layer during the early morning (also detected by the radiosonde launched at 07:30 UTC) and how around 09:00 UTC the mixed layer merges with the RL from the previous night producing a sudden increase of the boundary-layer depth. From this moment, the observed boundary-layer depth remains approximately constant for 7 hours. Taking into account that surface heat flux is still positive for several hours, this might be explained due to the existence of

subsidence that prevents the mixed layer to grow. During the afternoon, due to subsidence and the decrease of surface fluxes, UHF and radio sounding measurements show a slight decrease of the boundary-layer depth from 17:00 UTC.

DALES numerical experiments including the residual layer in their initial profile fit correctly the observations, simulating the sudden increase of the boundary-layer depth during the morning transition. On the other hand, DALES nRL numerical experiments simulate a progressive increase of the boundary-layer depth and underestimate by several hundred meters the observations during the whole morning, until 13:00 UTC. In all DALES results, small fluctuations on z_1 are observed at the end of the day (around 18:00 UTC) due to the cease of the surface heat flux, which produces fluctuations on the buoyancy flux vertical profile (Pino et al., 2006b).

Previous studies such as Fedorovich (1995) demonstrate that zeroth-order models can be also useful and valid to develop studies of the evolution of the boundary layer. In our study, the boundary-layer depth obtained with MLM has almost the same value as in DALES numerical experiments that include both the residual layer and subsidence confirming the studies previously developed.

Regarding the role of subsidence in the numerical experiments, it can be observed that the runs that include subsidence (RLs, nRLs, MLM) fit better with the observations but slightly underestimate the observed boundary-layer depth (less than 100 m with respect UHF measurements) maybe due to subsidence diurnal variability. The numerical experiments that do not consider subsidence overestimate the observed z_1 by less than 200 m. Long-term observations of the boundary layer show the importance of considering subsidence to obtain realistic approximations (Yi et al., 2001; Pietersen et al., 2014).

3.4 Morning entrainment heat flux

To understand the differences in the boundary-layer evolution between the numerical experiments during the morning, as the surface heat fluxes are the same, in this section we focus our analysis on the entrainment heat flux, keeping in mind the evolution of z_1 shown in Fig. 5 (see Eq. 1). Figure 6 shows the morning temporal evolution of heat flux at z_1 for the nRLns and RLns numerical experiments and the entrainment heat flux at the top of the RL (dotted line) to compare the entrainment heat flux at z_1 and z_{RL} before the inclusion of the RL. Several authors (Sorbjan, 1996; Sullivan et al., 1998; Conzemius and Fedorovich, 2006) pointed out the importance of the entrainment processes for the evolution of the potential temperature. Before 09:00 UTC, z_1 growth is similar in both simulations. Consequently, the difference of the entrainment heat flux between the numerical experiments is due to the potential temperature inversion jump (see Eq. 2); $\Delta\theta_1$ is 2 K larger for nRLns than for RLns at 08:30 UTC (see Fig. 3a). Therefore, larger entrainment heat flux is obtained

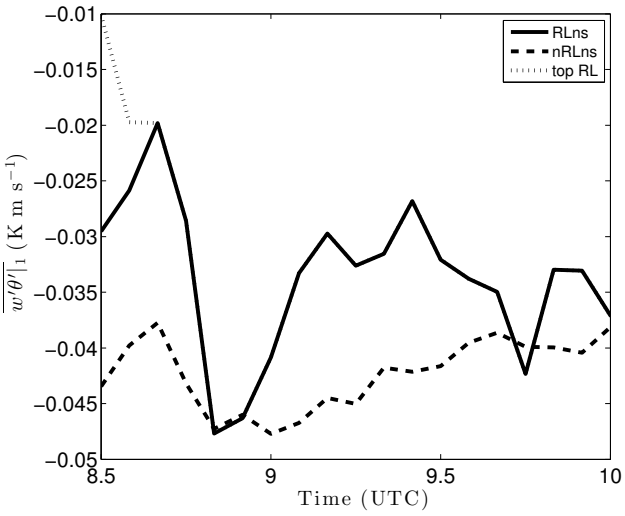

Fig. 6. Temporal evolution during the morning of the entrainment heat flux for the RLns (solid line), the entrainment heat flux at the top of the RL (pointed line) and nRLns (dashed line) DALES numerical experiments.

for the nRLns numerical experiment and the mixed-layer potential temperature increases more for this numerical experiment.

Just when the residual layer is incorporated into the boundary layer in the RLns numerical experiment, the entrainment heat flux must be nearly zero because the temperature jump is zero at the CBL (see Eq. 2). Then the residual layer is incorporated into the boundary layer, and the entrainment heat flux increases from -0.02 to $-0.045\,\mathrm{K\,m\,s^{-1}}$, introducing more air from the FA. This is mainly due to the increase of the potential temperature inversion jump (from nearly 0 to 1 K) and also to the large increase in the z_1 growth (see in Fig. 3a, b). From 10:00 UTC to the end of the simulation, entrainment heat flux for both DALES numerical experiments is similar (not shown).

3.5 Turbulent kinetic energy budget

Under horizontally homogeneous conditions, the turbulent kinetic energy (TKE) budget reads (Stull, 1988)

$$\frac{\partial \overline{e}}{\partial t} = -\left[\overline{w'u'}\frac{\partial u}{\partial z} + \overline{w'v'}\frac{\partial v}{\partial z}\right] + \frac{g}{\theta_{vr}}\overline{w'\theta'_v} - \\ -\frac{\partial \overline{w'e'}}{\partial z} - \frac{1}{\rho_0}\frac{\partial \overline{w'p'}}{\partial z} - \varepsilon, \quad (3)$$

where u', v', and w' are the turbulent fluctuations of the velocity components, p is the pressure, ρ_0 is a reference density, θ_{vr} is a reference virtual potential temperature, $\overline{e} = 0.5(\overline{u'^2 + v'^2 + w'^2})$ is the mean turbulent kinetic energy and ϵ is the viscous dissipation of TKE. The term on the left-hand side represents storage (STO) of TKE, and the terms on the right-hand side represent shear (S), and buoyancy production

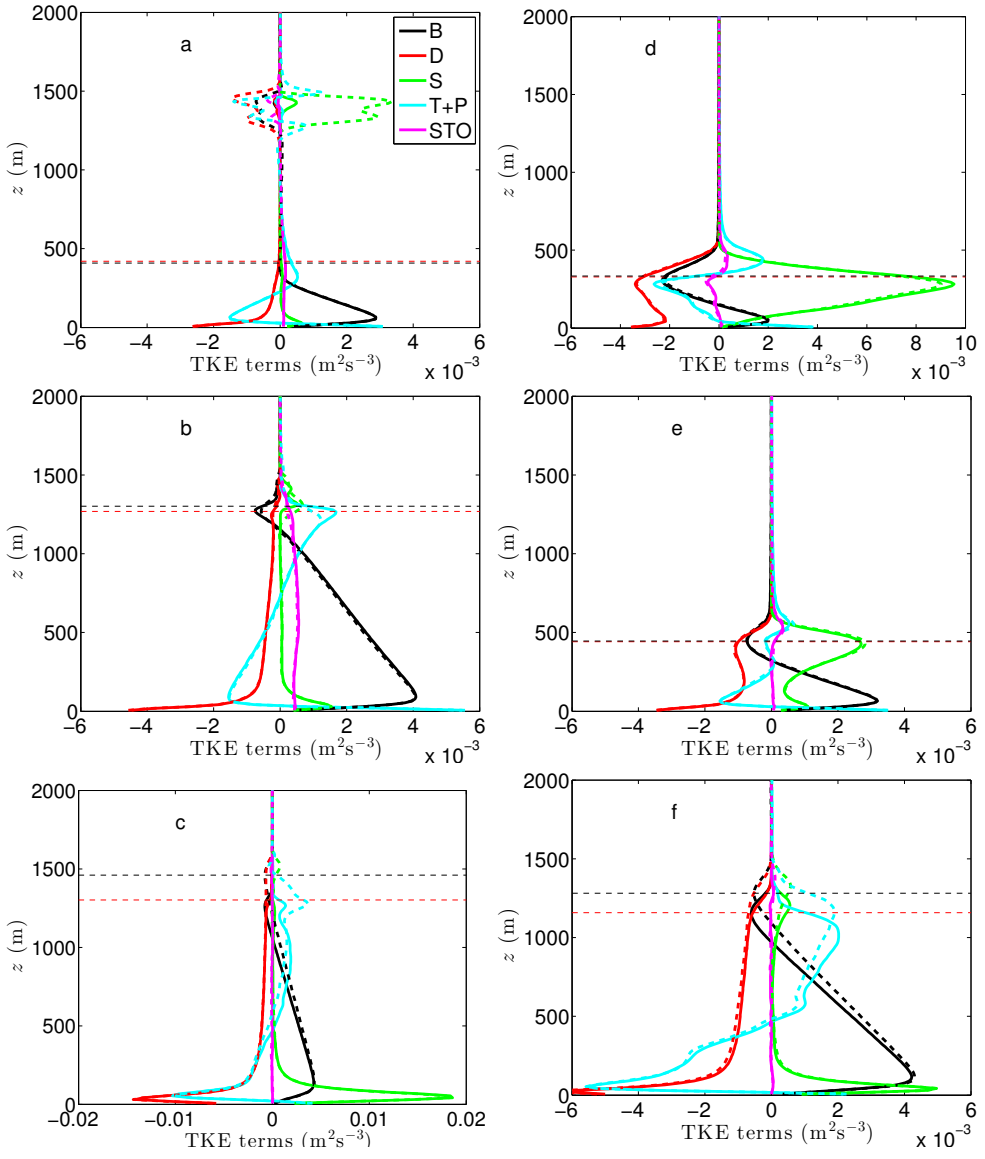

Fig. 7. Vertical profiles of the 30-min averaged TKE terms for the (left) RLns (dashed lines) and RLs (solid lines) and (right) nRLs (solid lines) and nRLns (dashed lines) numerical experiments at 08:30 (top), 09:00 (middle), and 14:00 UTC (bottom). Buoyancy production (black line), dissipation (red line), shear production (green line), turbulent transport and pressure (cyan line) and storage (magenta line) are shown. Red and black horizontal dashed lines mark the subsidence and no-subsidence cases z_1 averaged every 30 min.

(B), turbulent transport (T), pressure correlation (P), and viscous dissipation (D) terms.

Figure 7 shows the vertical profile of the averaged profile every 30 min of the different resolved TKE terms at 08:30 (top), 09:00 (middle), and 14:00 UTC (bottom) , for all the numerical experiments. The left panels show the numerical experiments where the residual layer is considered, whereas the right panels show those without the residual layer prescribed in the initial profile. The horizontal dashed lines mark z_1 for each numerical experiment. Notice the different range of the horizontal axis of Fig. 7c and d. Turbulent transport and the pressure correlation terms are plotted together as the convergence of the turbulence kinetic energy flux (Driedonks, 1982).

At 08:30 UTC (Fig. 7a, d), when the boundary layer is shallow for all the numerical experiments, we obtain larger values of all the TKE terms at the entrainment zone, but similar values of near the surface, for the nRL numerical experiments. At this moment, larger entrainment heat flux is simulated for nRL numerical experiments (see Fig. 6). Moreover, nRL presents larger momentum fluxes at z_1 (not shown) due to the difference setup regarding wind characteristics; a larger jump on the horizontal velocities is prescribed for nRL numerical experiments (see Table 1). To balance the budget,

the pressure-transport term and the dissipation term are also larger for the nRL numerical experiments, especially in the entrainment zone (compare Fig. 7a, d). As expected, the influence of subsidence cannot be noticed at this early hour because subsidence was prescribed increasing for surface, being maximum at z_{RL}. The TKE distribution of Fig. 7a and d was previously observed in the LES morning transition analysis by Beare (2008).

Focusing on Fig. 7a, at the top of the RL turbulence exists due to the interaction between this layer and the FA, which have different thermodynamic conditions. Smaller turbulence (S, T + P) and consequently dissipation are simulated at the top of the RL for RLs numerical experiment (solid lines) because subsidence reduces turbulence movements.

The effect of the inclusion of the residual layer into the mixed layer between 08:30 and 09:00 UTC can be clearly seen by comparing Fig. 7a and b, where the TKE terms of the both RL numerical experiments are represented. Shear and dissipation terms become approximately constant in the middle of the boundary layer, being larger at the inversion due to the larger potential temperature inversion jump. Consequently, the pressure-transport term increases in this zone. In Fig. 7b subsidence effect can be already observed producing a difference in z_1 around 50 m between RLns and RLs numerical experiments (compare red and black horizontal dashed lines). This fact can be compared with the nRL cases shown in Fig. 7e. In this figure the effect of subsidence is hardly observed due to the lower z_1 simulated at this hour for the nRL numerical experiments.

From 08:30 to 09:00 UTC, the value of TKE terms for the nRL numerical experiments (see Fig. 7d, e) decreases. This is due to the increase of boundary-layer depth and the reduction of the inversion strength at z_1 that primarily reduces buoyancy and shear terms at the inversion and, to balance the budget, the other terms.

At 14:00 UTC (Fig. 7c, f), similar z_1 is simulated for nRL and RL numerical experiments having the same subsidence conditions. Notice the differences in z_1 around 200 m between the numerical experiments due to subsidence. At this moment, STO, B and T+P terms are approximately similar for all numerical experiments (note the different range of the x axis between these two figures). However, larger S and, consequently, D terms are found for the RL numerical experiments near the surface. This is due to the fact that, from midday, when the boundary layer is similar for both numerical experiment, larger winds at the mixed layer are simulated for these numerical experiments.

In Fig. 7f the effect of subsidence in the different TKE terms can be analyzed. No differences between nRLs and nRLns can be observed in the lower part of the mixed layer. Additionally, subsidence plays an important role only in some of the TKE processes. In the mixed layer, subsidence hardly affects D, STO (very small) and S terms, and the main differences appear in B and T+P terms. Subsidence decreases buoyancy production in the upper mixed layer and consequently increases T+P term. In the entrainment zone, above z_1, if the areas of the TKE terms are compared, it can be concluded that similar values are obtained for the two numerical experiments.

Figure 8 shows the evolution every 5 min of the vertical integration from 0 to z_1 of each TKE term normalized by z_1. Note that the differences appearing in Fig. 8 between the different numerical experiments cannot be attributed to a smaller vertical integration domain. For the three presented cases – RLns, nRLns and nRLs – STO and T+P terms remain small when comparing with the other terms during the whole evolution, being negligible after the morning transition.

In Fig. 8a the effect of the inclusion of the residual layer is shown. Until approximately 10:00 UTC, nRLns (dashed lines) presents a larger shear, mainly occurring at the entrainment zone (see Fig. 7d), due to the prescribed initial wind profile (see Table 1, and Fig. 2c), but then reduces continuously because the mixed-layer wind speed in the nRLns experiment increases and reaches values close to the geostrophic wind. The increase of surface shear does not compensate for this fact. Before the inclusion of the RL, which can be clearly seen by the maximum of B integrated term around 09:00 UTC, RLns numerical experiment (solid lines) presents very small integrated S term due to initial prescribed wind profile (see Table 1 and Fig. 2c) that produces small wind shear at the surface and at the inversion zone during the first hours of the simulation. When the RL is incorporated, entrainment shear increases but the normalized integrated TKE is similar. Keep in mind that the integration is up to z_1, and as a consequence the shear above this height is not considered (see Fig. 7a, b, c). Afterwards, the integrated S term in RLns increases mainly due to the increase of surface shear due to the growth of mixed-layer wind speed. Entrainment shear for nRLns is reduced.

Regarding the integrated B, during the first hours of the simulation it is larger for RLns when comparing with nRLns (see Fig. 8a) because for this last numerical experiment much larger entrainment negative heat flux is simulated producing smaller vertically integrated B (see Fig. 6, 7a, d). Until 11:00 UTC, the integrated B term increases for both numerical experiments (surface and entrainment heat fluxes increase), becoming similar.

Before 11:00 UTC, the integrated D is slightly smaller for the RLns numerical experiment (solid lines). Later, integrated D remains almost constant for nRLns but increases for RLns until 11:00 UTC. At this time, the vertically integrated S and D terms are similar for both numerical experiments.

From midday the vertically integrated B term is similar for both numerical experiment because despite the fact that the respective boundary layer dephts are different until 15:00 UTC (see Fig. 5), and larger positive and negative heat fluxes are simulated for the nRLns numerical experiment (see Fig. 7c, f), its integration produces similar values. However, the vertically integrated S term decreases for the nRLns numerical experiment but continuously increases

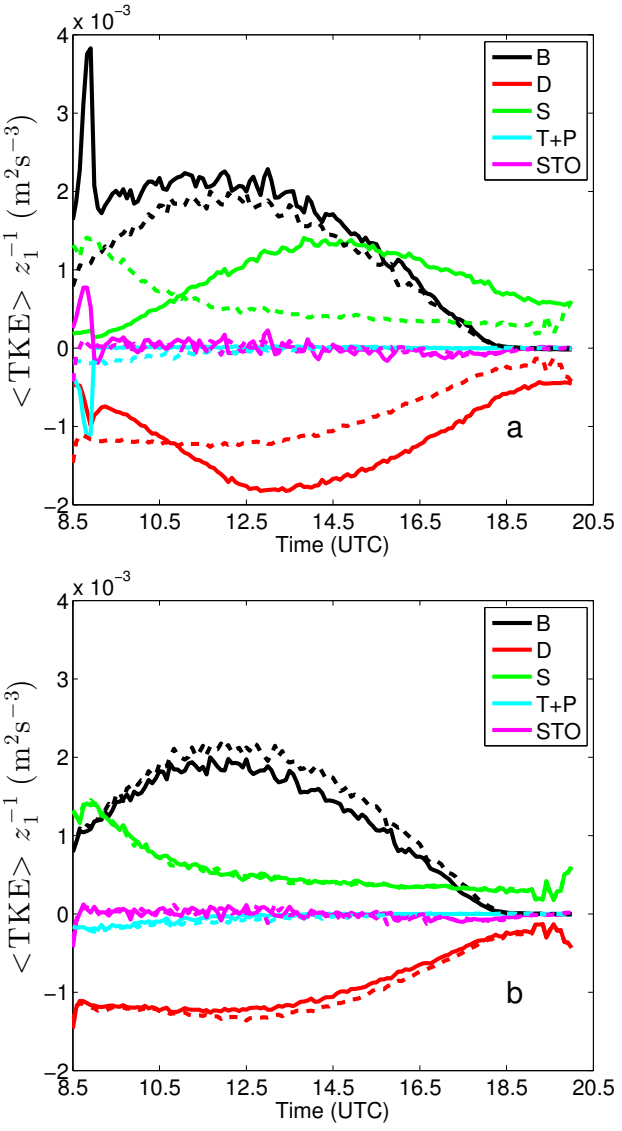

Fig. 8. Temporal evolution of each vertically averaged (from 0 to z_1) TKE term normalized by z_1. In **(a)** the influence of the RL is shown for (solid) RLns and (dashed) nRLns numerical experiments. In **(b)** the influence of subsidence for (dashed) nRLns and (solid) nRLs numerical experiments can be analyzed.

until 15:00 UTC for RLns for the reasons mentioned above. Consequently, to balance the TKE budget, larger vertically integrated D is also obtained for the RLns numerical experiment. From 15:00 UTC, surface and entrainment heat fluxes as well as entrainment momentum fluxes are quite low, and consequently the integration of all the TKE terms decreases.

The influence of the subsidence in the integrated TKE is analyzed for the nRL cases by observing Fig. 8b. It can be concluded that differences can be only noticed in the normalized integrated B term and to a lesser extent in the dissipation. Larger integrated buoyancy is simulated when subsidence is not considered (dashed black line), and this difference is mainly related with entrainment processes because if the same surface heat fluxes are prescribed for both numerical experiments, buoyancy flux is similar in the lower mixed layer for nRLs and nRLns. That is, the positive buoyancy flux is similar for nRLs and nRLns. Consequently, the lower the boundary layer depth is, the larger the integrated buoyancy flux is obtained because the entrainment buoyancy flux (negative flux) is smaller.

3.6 Influence of the residual layer on the observed evolution of the CO_2 mixing ratio

In this section, we analyze the importance of entrainment and surface CO_2 fluxes measured over different land uses in the evolution of the CO_2 mixing ratio. Some authors (de Arellano et al., 2004; Casso-Torralba et al., 2008) have analyzed the importance of entrainment CO_2 fluxes, which are especially relevant during early morning, but over homogenous terrains. Moreover, Moncrieff et al. (1997), Baldocchi et al. (1998) and Soegaard (1999) analyzed the evolution of the CO_2 mixing ratio over heterogeneous terrains during daily and longer periods of time. Here, we deal with CO_2 surface fluxes measured over different land uses and what their influence is on CO_2 mixing ratio in an evolving convective boundary layer.

Figure 9 shows the observed temporal evolution from 14:00 UTC on 30 June 2011 to 14:00 UTC on 1 July 2011 of the CO_2 mixing ratio and CO_2 flux measured at 2 m over different land uses (moor, corn and grass). As a reference, the measurements taken by the 30 m EC sensor located at the 60 m tower over grass are also included. Differences between CO_2 mixing ratio measurements over different land uses on 1 July 2011 are below 2 ppm during daytime and below 10 ppm during nighttime. By comparing 2 and 30 m measurements, differences of CO_2 mixing ratio are below 2 ppm at nighttime and below 12 ppm during daytime. In general during the night, larger CO_2 mixing ratio is observed near the surface than at 30 m over the same land use. Due to the large fluctuations of the measurements, this fact cannot be corroborated.

Between 05:00 and 09:00 UTC, a remarkable decrease of the CO_2 mixing ratio is observed at 2 m. At 30 m the decrease in CO_2 is less pronounced. Before 09:00 UTC, boundary layer is shallow (see Fig. 5), and the RL has not been incorporated yet to the mixed layer. During these hours surface uptake and mainly CO_2 entrainment flux drive the decrease of CO_2 mixing ratio (de Arellano et al., 2004; Casso-Torralba et al., 2008). Additionally, during early morning advection may also play a role. When entrainment flux mainly drives the decrease of CO_2 mixing ratio (around 06:00 UTC), the decrease is similar at both heights. Later on, when CO_2 surface fluxes become larger, differences appear between the CO_2 at 2 m and at 30 m. At 30 m, as expected the CO_2 surface flux is smaller, and, consequently, there is a smother decrease of the CO_2 mixing ratio at this altitude.

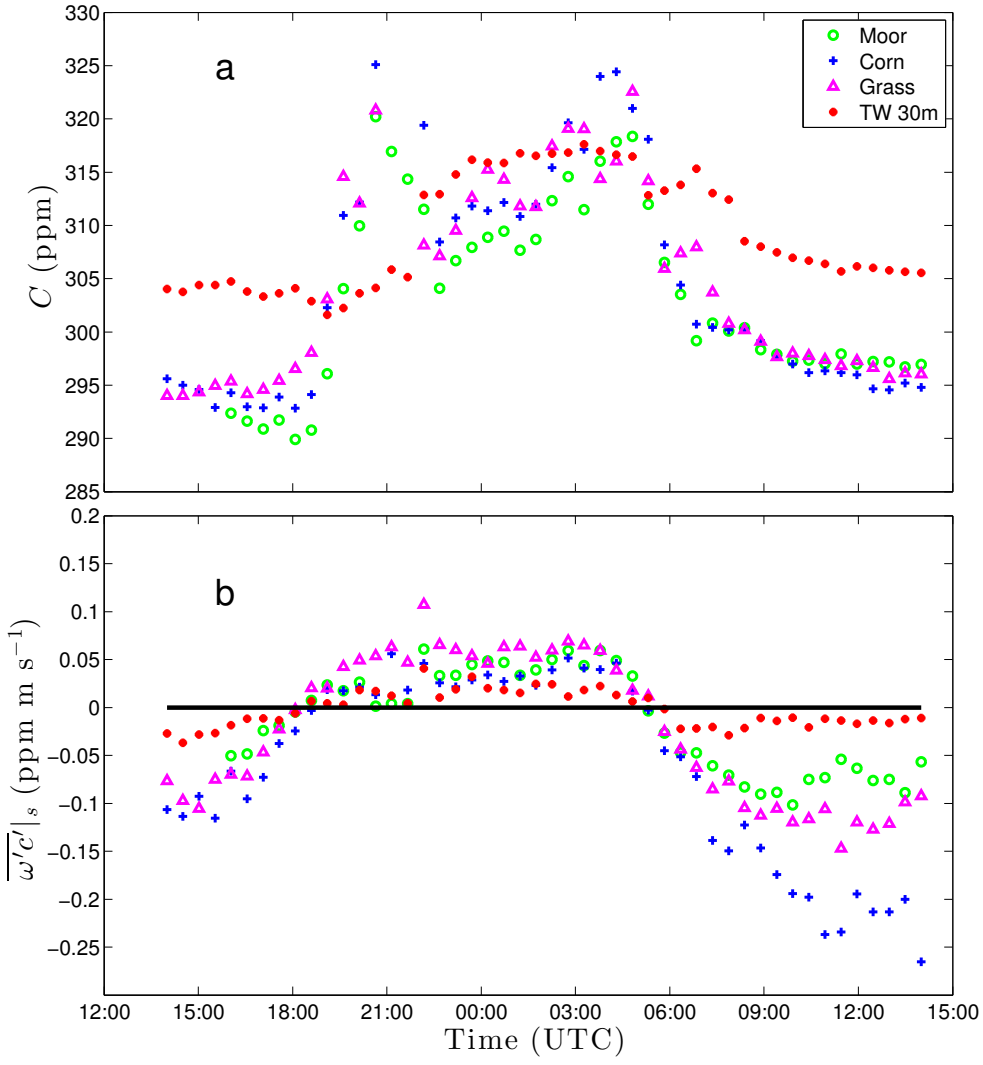

Fig. 9. Temporal evolution from 30 June 2011 at 14:00 UTC to 1 July 2011 at 14:00 UTC of the observed **(a)** CO_2 mixing ratio and **(b)** CO_2 surface flux measured at 2 m over moor (green circles), over corn (blue crosses), over long grass (magenta triangles) and at 30 m over grass (red asterisks).

During this IOP, no measurements of CO_2 entrainment flux were taken. However, since we have measurements of CO_2 surface flux, boundary-layer depth and temporal evolution of the CO_2 mixing ratio, in convective conditions, CO_2 entrainment flux can be estimated. By neglecting CO_2 advection and mean vertical velocity, the storage of CO_2 mixing ratio in the mixed layer reads

$$\frac{\partial \overline{c}}{\partial t} = \frac{\overline{\omega' c'}|_s - \overline{\omega' c'}|_1}{z_1}, \quad (4)$$

where $\overline{\omega' c'}|_s$ and $\overline{\omega' c'}|_1$ are the turbulent CO_2 flux at the surface and at z_1 (CO_2 entrainment flux), respectively, and $\overline{c}$ is the mean CO_2 mixing ratio in the mixed layer. By using Eq. (4), CO_2 entrainment flux can be calculated, which is 3 times larger than CO_2 surface flux before 09:00 UTC.

Once the RL is incorporated into the mixed layer, the boundary-layer depth increases suddenly to values close to 1300 m (see Fig. 5). As it was shown in Sect. 3.3, the boundary-layer growth is almost zero from that time. Therefore, CO_2 entrainment flux is almost negligible (Yi et al., 2001). After 09:00 UTC, it can be observed in Fig. 9a that CO_2 mixing ratio is around 297 ppm over all the surfaces, varying between 1 and 1.5 ppm, depending on the land use, for 3 h. However, clearer differences in the CO_2 surface fluxes are observed (see Fig. 7b). CO_2 mixing ratios present only slight variations because the observed z_1 from 09:00 UTC is large, and consequently $\overline{\omega' c'}|_s / z_1$ is small. For the land uses shown in Fig. 9, $\partial C/\partial t$ is around 0.3 ppm h^{-1} for moor and wheat, and close to 0.5 ppm h^{-1} for corn. Therefore, the mixing ratio is controlled almost by mixed

layer growth, with the surface flux playing not an important role (Culf, 1997; Pino et al., 2012).

From this analysis, we conclude that on 1 July 2011, before the merging of CBL and RL, CO_2 mixing ratio decreases from the high values of CO_2 observed during the night to the CO_2 mixing ratio of RL (CO_2 mixing ratio of the previous day) mainly due to CO_2 entrainment flux. This CO_2 mixing ratio is almost constant during the rest of the day due to the large and constant value of z_1.

4 Conclusions

The impact of the residual layer and subsidence on the evolution of a CBL is studied by means of observations taken during the BLLAST campaign, DALES numerical experiments and mixed-layer theory. In contrast with previous analysis of the morning transition (e.g., Angevine et al., 2001; LeMone et al., 2002; Lapworth, 2006; Beare, 2008), we use a sensitivity analysis of the the numerical experiments to study the influence of the two processes in the evolution of the convective boundary layer.

Depending on whether residual layer is considered or not in the DALES numerical experiments, different evolution of the boundary layer is simulated. Potential temperature simulated by the numerical experiments considering the residual layer fits correctly the observations in contrast with numerical experiments without residual layer (nRL), which simulate a too large mixed-layer heating rate during the early morning. By using mixed-layer theory, we conclude that the difference in the evolution of the potential temperature is due to entrainment heat flux, because we prescribed the same surface fluxes for all the numerical experiments and the z_1 growth is similar before the morning transition. After the merge of residual layer and CBL, large entrainment heat flux is simulated in the numerical experiments with residual layer because $\Delta\theta_1$ and $\partial z_1/\partial t$ also increase.

For DALES numerical experiments including the residual layer, a rapid increase of boundary-layer depth is obtained, similar to observations, when the residual layer is incorporated in the mixed layer. In contrast, boundary-layer depth for the numerical experiments without residual layer grows at a lower rate, underestimating it relatively to the observations by several hundred meters until 13:00 UTC.

Subsidence also plays an important role in the evolution of the CBL. Without subsidence included in the simulations, the simulated boundary layer depth continues to grow reaching higher values than the observed. Moreover, we compare different initializations of subsidence: DALES with a simple vertical profile and MLM with a subsidence value defined at the top of the CBL. The evolutions of the boundary-layer depths are similar with both initializations, and in agreement with the observations verifying the practicality and effectiveness of simpler models.

DALES allows us to evaluate the influence of the residual layer in the TKE budget during the whole day. When the residual layer is taken into account, buoyancy, pressure transport and dissipation are the largest terms before the inclusion of the residual layer (before 09:00 UTC). When it is incorporated into the mixed-layer, buoyancy and shear increase at the inversion and near the surface. On the contrary, if residual layer is not considered, TKE terms present the typical evolution during boundary layer growth (Pino and Vilà-Guerau de Arellano, 2008).

The effect of subsidence in the evolution of the TKE terms is less pronounced. Subsidence influence is restricted to the upper part of the mixed layer and to the entrainment zone. In this region the effect of subsidence can be clearly observed in the buoyancy and pressure-transport terms. Subsidence decreases the turbulence production decreasing buoyancy in the upper mixed-layer but increases the contribution of pressure-transport term.

Regarding the vertical integration of the TKE terms, the differences between the numerical experiments with or without residual layer are mainly due to the shear term. During the first hours of the simulations, the differences in the shear term (larger for nRL numerical experiments) are related to the different prescription of the initial wind profile. Afterwards, normalized integrated S term decreases for nRL mainly because entrainment shear decreases. On the contrary, S term increases in RL because larger surface shear is simulated as the wind speed in the boundary layer increases.

We also analyze the influence of the residual layer in the evolution of CO_2 mixing ratio by using the observations. Before 09:00 UTC, CO_2 surface fluxes are small, the boundary layer is shallow, and CO_2 mixing ratio decrease is mainly driven by CO_2 entrainment flux. After the inclusion of the residual layer into the mixed layer, the boundary layer depth is almost constant during the rest of the day. Therefore CO_2 entrainment flux is very small and, despite the larger observed CO_2 surface flux observed over some surfaces, the CO_2 mixing ratio is very similar over the different land uses because storage term is below 0.5 ppm h^{-1} over all the surfaces due to the large value of z_1.

We conclude that a precise definition of the characteristics of the residual layer is fundamental, even though it is complex because the evolution of the main variables in the residual layer during the previous night depends on different factors such as advection or subsidence, which can change in time.

Acknowledgements. This work was supported by Spanish MINECO projects CGL2009-08609, and CGL2012-37416-C04-03. DALES simulations were performed at SARA with the financial support of the project NCF-NWO SH-060-09. The MODEM radio sounding station and the UHF wind profiler have been supported by CNRS, Université Paul Sabatier and FEDER program (contract no. 34172 – Development of the instrumentation of Observatoire Midi-Pirénées-PIRENEA-ESPOIR). The 60 m tower equipment has

been supported by CNRS, Université Paul Sabatier and European POCTEFA 720 FluxPyr program. One EC station was supported by Wageningen University, and two EC stations were supported by the University of Bonn and DFG project SCHU2350/21.

BLLAST field experiment was made possible thanks to the contribution of several institutions and supports: INSU-CNRS (Institut National des Sciences de l'Univers, Centre National de la Recherche Scientifique, LEFE-IDAO program), Météo-France, Observatoire Midi-Pirénées (University of Toulouse), EUFAR (EUropean Facility for Airborne Research) and COST ES0802 (European Cooperation in the field of Scientific and Technical). The field experiment would not have occurred without the contribution of all participating European and American research groups, which all have contributed in a significant amount. BLLAST field experiment was hosted by the instrumented site of Centre de Recherches Atmosphériques, Lannemezan, France (Observatoire Midi-Pirénées, Laboratoire d'Aérologie). BLLAST data are managed by SEDOO, from Observatoire Midi-Pirénées.

Edited by: R. J. Beare

References

Angevine, W. M.: Transitional, entraining, cloudy, and coastal boundary layers, Acta Geophys., 56, 2–20, 2007.

Angevine, W. M., Baltink, H. K., and Bosveld, F. C.: Observations of the morning transition of the convective boundary layer, Bound.-Lay. Meteorol., 101, 209–227, 2001.

Angevine, W. M., White, A. B., and Avery, S. K.: Boundary-layer depth and entrainment zone characterization with a boundary-layer profiler. Bound.-Lay. Meteorol., 68(4), 375–385, 1994.

Baldocchi, D. and Meyers, T.: On using eco-physiological, micrometeorological and biogeochemical theory to evaluate carbon dioxide, water vapor and trace gas fluxes over vegetation: a perspective, Agr. Forest Meteorol., 90, 1–25, 1998.

Balin, I., Parlange, M., Calpini, B., Simeonov, V., and van den Bergh, H.: Elevated atmospheric boundary layer over the Swiss Alps during the August 2003 heat wave, 22nd Internation Laser Radar Conference, Matera, Italy, 12–16 July, 561, 2004.

Balsley, B. B., Svensson, G., and Tjernström, M.: On the scale-dependence of the gradient Richardson number in the residual layer, Bound.-Lay. Meteorol., 127, 57–72, 2007.

Bange, J., Spieß, T., and van den Kroonenberg, A.: Characteristics of the early-morning shallow convective boundary layer from Helipod flights during STINHO-2, Theor. Appl. Climatol. 90, 113–126, 2006.

Beare, R. J.: The role of shear in the morning transition boundary layer, Bound.-Lay. Meteorol., 129(3), 395–410, 2008.

Beare, R. J., Edwards, J. M., and Lapworth, A. J.: Simulation of the observed evening transition and nocturnal boundary layers: large-eddy modelling, Q. J. Roy. Meteorol. Soc., 132, 61–80, 2006.

Carlson, M. A. and Stull, R.: Subsidence in the nocturnal boundary layer, J. Clim. Appl. Meteorol. 25, 1088–1099, 1986.

Carson, D. J.: The development of a dry inversion-capped convectively unstable boundary layer, Q. J. Roy. Meteorol. Soc., 99, 450–467, 1973.

Casso-Torralba, P., Vilà-Guerau de Arellano, J., Bosveld, F. C., Soler, M. R., Vermeulen, A., Werner, C., and Moors, E. : Diurnal and vertical variability of the sensible heat and carbon dioxide budgets in the atmospheric surface layer, J. Geophys. Res., 113, D12119, doi:10.1029/2007JD009583, 2008.

Cohn, S. A. and Angevine, W. M.: Boundary layer height and entrainment zone thickness measured by lidars and wind-profiling radars, J. Appl. Meteorol., 39, 1233–1247, 2000.

Cole, G. S. and Fernando, H. J. S.: Some aspects of the decay of convective turbulence, Fluid Dyn. Res., 23, 161–176, 1998.

Conzemius, R. J. and Fedorovich, E.: Dynamics of sheared convective boundary layer entrainment. Part I: Methodological background and large-eddy simulations, J. Atmos. Sci., 63(4), 1151–1178, 2006.

Conzemius, R. J. and Fedorovich, E.: Bulk models of the sheared convective boundary layer: evaluation through Large Eddy Simulations, J. Atmos. Sci., 64, 786–807, 2007.

Culf, A. D., Fisch, G., Malhi, Y. and Nobre, C. A.: The influence of the atmospheric boundary layer on carbon dioxide concentrations over a tropical forest. Agr. Forest Meteorol., 85, 149–158, 1997.

Cuijpers, J. W. M. and Duynkerke, P. G.: Large eddy simulation of trade wind cumulus clouds. J. Atmos. Sci., 50(23), 3894–3908, 1993.

de Arellano, J. V.-G., Gioli, B., Miglietta, F., Jonker, H. J. J., Baltink, H. K., Hutjes, R. W. A., and Holtslag, A. A. M.: Entrainment process of carbon dioxide in the atmospheric boundary layer, J. Geophys. Res., 109, D18110, doi:10.1029/2004JD004725, 2004.

De Coster, O. M. Y. and Pietersen, H. P.: BLLAST-uniform processing of Eddy-Covariance data. Internship Report Meteorology and Climatology, Wageningen University and Research Center, The Netherlands, 30 pp., available at: http://bllast.sedoo.fr/documents/reports/H-Pietersen_O-de-Coster_BLLAST-surf_flx-uniform-processing.pdf, 2011.

Deardorff, J. W., Willis, G. E., and Stockton, B. H.: Laboratory studies of the entrainment zone of a convectively mixed layer, J. Fluid Mech., 100(01), 41–64, 1980.

Doran, J. C., Berkowitz, C. M., Coulter, R. L., Shaw, W. J., and Spicer, C. W.: The 2001 Phoenix Sunrise experiment: vertical mixing and chemistry during the morning transition in Phoenix, Atmos. Environ., 37, 2365–2377, 2003.

Driedonks, A. G. M.: Models and observations of the growth of the atmospheric boundary layer. Bound.-Lay. Meteorol., 23), 283–306, 1982.

Edwards, J. M., Beare, R. J., and Lapworth, A. J.: Simulation of the observed evening transition and nocturnal boundary layers: Single-column modelling, Q. J. Roy. Meteorol. Soc., 132, 61–80, 2006.

Emeis, S. and Schäfer, K.: Remote sensing methods to investigate boundary-layer structures relevant to air pollution in cities, Bound.-Lay. Meteorol., 121, 377–385, 2006.

Fedorovich, E.: Modeling the atmospheric convective boundary layer within a zero-order jump approach: An extended theoretical framework, J. Appl. Meteorol., 34, 1916–1928, 1995.

Fedorovich, E., Kaiser, R., Rau, M., and Plate, E.: Wind tunnel study of turbulent flow structure in the convective boundary layer capped by a temperature inversion, J. Atmos. Sci., 53, 1273–1289, 1996.

Fedorovich, E., Nieuwstadt, F. T. M., and Kaiser, R.: Numerical and laboratory study of a horizontally evolving convective boundary

layer – Part I: Transition regimes and development of the mixed layer, J. Atmos. Sci., 58, 70–86, 2001.

Fochesatto, G. J., Drobinski, P., Flamant, C., Guedalia, D., Sarrat, C., Flamant, P. H., and Pelon, J.: Evidence of dynamical coupling between the residual layer and the developing convective boundary layer, Bound.-Lay. Meteorol., 99, 451–464, 2001.

Garai, A., Pardyjak, E. R., Steeneveld, G.-J., and Kleissl, J.: Surface temperature and surface-layer turbulence in a convective boundary layer. Bound.-Lay. Meteorol., 148(1), 51–72, 2013.

Gibert, F., Arnault, N., Cuesta, J., Plougonven, R., and Flamant, P. H.: Internal gravity waves convectively forced in the atmospheric residual layer during the morning transition, Q. J. Roy. Meteorol. Soc., 137, 1610–1624, 2011.

Han, B., Lü, S., and Ao, Y.: Development of the convective boundary layer capping with a thick neutral layer in Badanjilin: Observations and simulations, Adv. Atmos. Sci., 29, 177–192, 2011.

Heus, T., van Heerwaarden, C. C., Jonker, H. J. J., Siebesma, A. P., Axelsen, S., van den Dries, K., Geoffroy, O., Moene, A. F., Pino, D., de Roode, S. R., and Vilà-Guerau de Arellano, J.: Formulation of the Dutch atmospheric large-eddy simulation (DALES) and overview of its applications, Geosci. Model Dev., 3, 415–444, doi:10.5194/gmd-3-415-2010, 2010.

Kaimal, J. C., Wyngaard, J. C., Haugen, D. A., Coté, O. R., Izumi, Y., Caughey, S. J., and Readings, C. J.: Turbulence structure in the convective boundary layer, J. Atmos. Sci., 33, 2152–2169, 1976.

Lapworth, A.: The morning transition of the nocturnal boundary layer, Bound.-Lay. Meteorol., 119, 501–526, 2006.

LeMone, M. A., Zhou, M., Moeng, C.-H., Lenschow, D. H., Miller, L. J. and Grossman, R. L.: An observational study of wind profiles in the baroclinic convective mixed layer, Bound.-Lay. Meteorol., 90, 47–82, 1999.

LeMone, M. A., Grossman, R. L., Mcmillen, R. T., Liou, K.-N., Ou, S. C., Mckeen, S., Angevine, W., Ikeda, K., and Chen, F.: CASES-97: Late-morning warming and moistening of the convective boundary layer over the Walnut River watershed, Bound.-Lay. Meteorol., 104, 1–52, 2002.

Lilly, D. K.: Models of cloud-topped mixed layers under a strong inversion, Q. J. Roy. Meteorol. Soc., 94, 292–309, 1968.

Lloyd, J. and Taylor, J. A.: On the temperature dependence of soil respiration, Funct. Ecol., 8, 315–323, 1994

Lothon, M., Lohou, F., Pino, D., Couvreux, F., Pardyjak, E. R., Reuder, J., Vilà-Guerau de Arellano, J., Durand, P., Hartogensis, O., Legain, D.,. Augustin, P, Faloona, I., Alexander, D. C., Angevine, W. M., Bargain, E., Barrié, J., Bazile, E., Bezombes, Y., Blay-Carreras, E., van de Boer, A., Boichard, J.-L., Bourdon, A., Butet, A., Campistron, B., de Coster, O., Cuxart, J., Dabas, A., Darbieu, C., Deboult, K., Delbarre, H., Derrien, S., Flament, P., Fourmentin, M., Garai, A., Gioli, B., Groebner, J., Guichard, F., Jimenez, M. A., Jonassen, M., van de Kroonenberg, A., Lenschow, D. H., Magliulo, E., Martin, S., Martinez, D., Mastrotillo, L., Moene, A. F., Molinos, F., Moulin, E., Pietersen, H. P., Piguet, B., Pique, E., Román-Cascón, C., Rufin-Soler, C., Saïd, F., Sastre-Marugán, M., Seity, Y., Steeneveld, G.-J., Toscano, P., Traullé, O., Tzanos, D., Yagüe, C., Wacker, S., Wildmann, N., and Zaldei, A.: The BLLAST field experiment: Boundary-Layer Late Afternoon and Sunset Turbulence, Atmos. Chem. Phys. Discuss., in press, 2014.

Mahrt, L.: Nocturnal boundary-layer regimes, Bound.-Lay. Meteorol., 88, 255–278, 1998.

Moeng, C.-H.: A large-eddy-simulation model for the study of planetary boundary-layer turbulence, J. Atmos. Sci., 41, 2052–2062, 1984.

Moeng, C.-H. and Sullivan P. P.: A comparison of shear- and buoyancy-driven planetary boundary layer flows. J. Atmos. Sci., 51, 999–1022, 1994.

Moncrieff, J., Monteny, B., Verhoef, A., Friborg, T., Elbers, J., Kabat, P., de Bruin, H., Soegaard, H. and Taupin, J. D.: Spatial and temporal variations in net carbon flux during HAPEX-Sahel, J. Hydrol., 189, 563–588, 1997.

Morris, G. A., Ford, B., Rappenglück, B., Thompson, A. M., Mefferd, A., Ngan, F., and Lefer, B.: An evaluation of the interaction of morning residual layer and afternoon mixed layer ozone in Houston using ozonesonde data, Atmos. Environ., 44, 4024–4034, 2010.

Nadeau, D. F., Pardyjak, E. R., Higgins, C. W., Fernando, H. J. S., and Parlange, M. B.: A simple model for the afternoon and early evening decay of convective turbulence over different land surfaces, Bound.-Lay. Meteorol., 141, 301–324, 2011.

Nieuwstadt, F. T. M.: The turbulent structure of the stable, nocturnal boundary layer, J. Atmos. Sci., 41, 2202–2216, 1984.

Nieuwstadt, F. T. M. and Brost R. A.: The decay of convective turbulence, J. Atmos. Sci., 43, 532–546, 1986.

Ouwersloot, H. G., Vilà-Guerau de Arellano, J., Nölscher, A. C., Krol, M. C., Ganzeveld, L. N., Breitenberger, C., Mammarella, I., Williams, J., and Lelieveld, J.: Characterization of a boreal convective boundary layer and its impact on atmospheric chemistry during HUMPPA-COPEC-2010. Atmos. Chem. Phys., 12, 9335–9353, doi:10.5194/acp-12-9335-2012, 2012.

Pietersen, H., Vilà-Guerau de Arellano, J., Augustin, P., de Coster, O., Durand, P., Gioli, B., Hartogensis, O., Lothon, M., Lohou, F., Pino, D., Ouwersloot, H. G., Reuder, J. and van de Boer, A.: Study of a prototypical convective boundary layer observed during BLLAST: contributions by large-scale forcing, to be submitted to Atmos. Chem. Phys. Discuss., 2014.

Pino, D., Vilà-Guerau de Arellano, J., and Duynkerke, P. G.: The contribution of shear to the evolution of a convective boundary layer, J. Atmos. Sci., 60, 1913–1926, 2003.

Pino, D., Vilà-Guerau de Arellano, J., and Kim, S. W.: Representing sheared convective boundary layer by zeroth- and first-order-jump mixed-layer models: Large-eddy simulation verification. J. Appl. Meteorol. Climatol., 45, 1224–1243, 2006a.

Pino, D., Jonker, H. J. J., Vilà-Guerau de Arellano, J., and Dosio, A.: Role of shear and the inversion strength during sunset turbulence over land: Characteristic length scales, Bound.-Lay. Meteorol., 121, 537–556, 2006b.

Pino, D. and Vilà-Guerau de Arellano, J.: Effects of shear in the convective boundary layer: analysis of the turbulent kinetic energy budget, Acta Geophys., 56, 167–193, 2008.

Pino, D., Vilà-Guerau de Arellano, J., Peters, W., Schröter, J., van Heerwaarden, C. C. and Krol, M. C.: A conceptual framework to quantify the influence of convective boundary layer development on carbon dioxide mixing ratio Atmos. Chem. Phys., 12, 2969–2985, doi:10.5194/acp-12-2969-2012, 2012.

Seibert, P., Beyrich, F., Gryning, S. E., Joffre, S., Rasmussen, A., and Tercier, P.: Review and intercomparison of operational meth-

ods for the determination of the mixing height, Atmos. Environ., 34, 1001–1027, 2000.

Soegaard, H.: Fluxes of carbon dioxide, water vapour and sensible heat in a boreal agricultural area of Sweden – scaled from canopy to landscape level, Agr. Forest Meteorol., 98–99, 463–478, 1999.

Sorbjan, Z.: Effects caused by varying the strength of the capping inversion based on a large eddy simulation model of the shear-free convective boundary layer, J. Atmos. Sci., 53, 2015–2024, 1996.

Sorbjan, Z.: Decay of convective turbulence revisited, Bound.-Lay. Meteorol., 82, 503–517, 1997.

Sorbjan, Z.: A numerical study of daily transitions in the convective boundary layer, Bound.-Lay. Meteorol., 123, 365–383, 2007.

Stensrud, D. J.: Elevated residual layers and their influence on surface boundary-layer evolution, J. Atmos. Sci., 50, 2284–2293, 1993.

Stull, R. B.: An Introduction to Boundary Layer Meteorology. Kluwer Academic Publisher, Dordrecht, the Netherlands, 670 pp., 1988.

Sullivan, P. P., Moeng, C.-H., Stevens, B., Lenschow, D. H., and Mayor, S. D.: Structure of the entrainment zone capping the convective atmospheric boundary layer, J. Atmos. Sci., 55, 3042–3064, 1998.

Tennekes, H.: A model for the dynamics of the inversion above a convective boundary layer, J. Atmos. Sci., 30, 558–567, 1973.

Tennekes, H. and Driedonks, A. G. M.: 1981, Basic entrainment equations for the atmospheric boundary layer, Bound.-Lay. Meteorol., 20, 515–531.

Vilà-Guerau de Arellano, J., van den Dries, K., and Pino, D.: On inferring isoprene emission surface flux from atmospheric boundary layer concentration measurements, Atmos. Chem. Phys., 9, 3629–3640, doi:10.5194/acp-9-3629-2009, 2009.

Wehner, B., Siebert, H., Ansmann, A., Ditas, F., Seifert, P., Stratmann, F., Wiedensohler, A., Apituley, A., Shaw, R. A., Manninen, H. E., and Kulmala, M.: Observations of turbulence-induced new particle formation in the residual layer, Atmos. Chem. Phys., 10, 4319–4330, doi:10.5194/acp-10-4319-2010, 2010.

Yi, C., Davis, K. J., Berger, B. W., and Bakwin P. S.: Long-term observations of the dynamics of the continental planetary boundary layer, J. Atmos. Sci., 58, 1288–1299, 2001.